

# Shock wave collisions in $AdS_5$ : approximate numerical solutions

Bin Wu<sup>1,2,3</sup> and Paul Romatschke<sup>1,4</sup>

<sup>1</sup>*Frankfurt Institute for Advanced Studies, D-60438 Frankfurt, Germany*

<sup>2</sup>*Faculty of Physics, University of Bielefeld, D-33501 Bielefeld, Germany*

<sup>3</sup>*School of Physics and State Key Laboratory of Nuclear Physics and Technology,  
Peking University, Beijing 100871, China*

<sup>4</sup>*Department of Physics, 390 UCB,  
University of Colorado, Boulder, CO 80309, USA*

## Abstract

We numerically study the evolution of a boost-invariant  $\mathcal{N} = 4$  SYM medium using AdS/CFT. We consider a toy model for the collision of gravitational shock waves, finding that the energy density first increases, reaches a maximum and then starts to decrease, matching hydrodynamics for late times. For the initial conditions we consider, the hydrodynamic scale governing the late time behaviour is to very good approximation determined by the area of the black hole horizon at initial times. Our results provide a toy model for the early time evolution of the bulk system in heavy-ion collisions at RHIC and the LHC.

## I. INTRODUCTION

The problem of colliding gravitational shock waves in spaces that are asymptotically Anti-de-Sitter has been of recent interest because it can serve as a toy model of the collision of two nuclei approaching at very high speeds. Hence it may provide — via the AdS/CFT conjecture [1, 2] — some qualitative insight in phenomena found in heavy-ion experiments at the Relativistic Heavy-Ion Collider (RHIC) and the Large Hadron Collider (LHC).

Boosting a mass at rest to very high velocities, its energy-momentum tensor in coordinates  $x^\pm = \frac{t \pm z}{\sqrt{2}}$  becomes that of a gravitational shock wave, e.g.  $T_{++} \propto \mu \delta(x^+)$ , where  $\mu$  is the energy per unit area which for a nucleus of atomic number  $a$ , radius  $R$  and Lorentz boost factor  $\gamma = \frac{\sqrt{s_{NN}}}{2m_p}$  is

$$\mu \propto \gamma \frac{am_p}{\pi R^2} = \frac{a\sqrt{s_{NN}}}{2\pi R^2}, \quad (1.1)$$

where  $m_p$  is the proton mass. It is well known how to model such an energy-momentum tensor using the AdS/CFT correspondence, namely by a metric of the form [3] (cf.[4–6])

$$ds^2 = \frac{-2dx^+dx^- + \phi(z)\delta(x^+)dx^{+2} + dx_\perp^2 + dz^2}{z^2} \quad (1.2)$$

where  $\phi(z) = \frac{\mu z^4}{\kappa}$  and we have set the *AdS* radius to unity. Here the description assumes the conjectured duality between  $\mathcal{N} = 4$  SYM at large coupling and large number of colours  $N_c$  and classical gravity on  $AdS_5 \times S^5$ . Since  $\mathcal{N} = 4$  SYM is a gauge theory, it behaves qualitatively similar to QCD, so some aspects of this work may translate to qualitatively similar phenomena found in nature. The constant  $\kappa$  is usually set to  $\frac{N_c^2}{2\pi^2}$ , but we will treat  $\kappa$  as a free parameter to be adjusted at will in order to obtain a model that more closely resembles QCD.

A collision of two nuclei can be modelled by a superposition of two shock waves in  $AdS_5$ , moving in  $x^+$  and  $x^-$  direction, respectively. While the line element before the collision is a simple superposition of the individual shock waves, the metric after the collision is in general hard to find. Unfortunately, while exact analytic solutions in four dimensional asymptotic Minkowski time have been derived many years ago [7], no such solutions are known for shock waves of the form (1.2). Therefore, one has to resort to numerical techniques, which were pioneered in [8, 9], see also [10, 11].

Another aspect of Eq. (1.2) is that the collision of two such shock waves can be shown to violate Bjorken’s conjectured invariance under rapidity boosts ([3]). Since experimental

data for heavy-ion collisions does not seem to back up this invariance either, this can be considered a feature rather than a shortcoming of the present model, but at the price that the gravitational dynamics is 2+1 dimensional (rapidity, AdS radius and time) [10] rather than 1+1 dimensional.

However, as we shall point out in the present work, it turns out that in the limit of weak shock waves  $\mu \ll 1$ , the leading order dynamics is in fact boost-invariant (cf. Ref. [12]). The late-time behavior of such a strongly coupled boost-invariant  $\mathcal{N} = 4$  SYM medium has been known up to the  $3^{rd}$  order in large  $\tau$  expansion [13–16]. However, one has to use numerical methods to fully understand the early-time properties of the system [17]. In this paper we use algorithms similar to those in Refs. [8, 9] to solve Einstein’s equations numerically in this approximation, and follow the evolution of the boundary energy-momentum tensor from the far-from equilibrium situation at early times to the hydrodynamic behavior at late times. Unlike Ref. [8, 9], we do not deform the boundary four dimensional metric of the  $AdS_5$  space but connect initial conditions derived analytically from the shock waves before the collision to the late time hydrodynamic regime. Our findings validate those of Ref. [11], where the authors use a different algorithm and start with arbitrary initial conditions.

This paper is organized as follows. In Sec. II we construct an ansatz metric function based on the approximate metric functions in the collisions of two weak shock waves. In Sec. III two algorithms for numerically solving Einstein’s equations in the bulk of the  $AdS_5$  space are described in detail. Our numerical results and an application to RHIC and LHC are presented in Secs. IV, V. In the Appendix A provide near-boundary power series expansions needed in our numerical calculations.

## II. COLLISIONS OF TWO WEAK SHOCK WAVES

The line element (1.2) is highly singular at  $x^\pm = 0$ , and it is useful to first change to so-called Rosen coordinates  $x^+ = u$ ,  $x^- = v + \frac{1}{2}\phi(\tilde{z})\theta(u) + \frac{1}{8}(\phi'(\tilde{z}))^2 u\theta(u)^2$ ,  $z = \tilde{z} + \frac{1}{2}\phi'(\tilde{z})u\theta(u)$ , with the result

$$ds^2 = \frac{-2dudv + dx_\perp^2 + \left(1 + \frac{1}{2}\phi''(\tilde{z})u\theta(u)\right)^2 d\tilde{z}^2}{\left(\tilde{z} + \frac{1}{2}\phi'(\tilde{z})u\theta(u)\right)^2}. \quad (2.1)$$

The collision of two shocks can be set up by superposing the above line element for one shock with an equivalent one for the other shock. The difficult part of the calculation then

involves finding the line element in the forward light-cone. Using the standard matching conditions (metric needs to be continuous and piece-wise differentiable [7]) it has been possible to find the metric in the approximation of small strength  $\mu$  [3]. Using the coordinates proper time  $\tilde{\tau} = \sqrt{2uv}$  and space-time rapidity  $\tilde{\eta} = \frac{1}{2} \ln \frac{u}{v}$  the result is given by [3]

$$ds^2 = \frac{-[1 + K(\tilde{\tau}, \tilde{\eta}, \tilde{z})] d\tilde{\tau}^2 + [1 + L(\tilde{\tau}, \tilde{\eta}, \tilde{z})] \tilde{\tau}^2 d\tilde{\eta}^2 + [1 + H(\tilde{\tau}, \tilde{\eta}, \tilde{z})] d\mathbf{x}_\perp^2}{\tilde{z}^2 [1 + 2\tilde{z}^2 \bar{\mu} \tilde{\tau} \cosh(Y - \tilde{\eta})]^2} + \frac{[1 + M(\tilde{\tau}, \tilde{\eta}, \tilde{z})] [1 + 6\tilde{z}^2 \bar{\mu} \tilde{\tau} \cosh(Y - \tilde{\eta})]^2 d\tilde{z}^2}{\tilde{z}^2 [1 + 2\tilde{z}^2 \bar{\mu} \tilde{\tau} \cosh(Y - \tilde{\eta})]^2}, \quad (2.2)$$

where  $\bar{\mu} = \mu/\kappa$  and  $K, L, H, M$  were determined to be

$$\begin{aligned} K(\tilde{\tau}, \tilde{\eta}, \tilde{z}) &= c_1 \bar{\mu}^2 \tilde{\tau}^2 \tilde{z}^4 - \frac{5 + c_1}{3} \bar{\mu}^2 \tilde{\tau}^4 \tilde{z}^2 + \mathcal{O}(\bar{\mu}^3) \\ L(\tilde{\tau}, \tilde{\eta}, \tilde{z}) &= \frac{-16 + c_1}{3} \bar{\mu}^2 \tilde{\tau}^2 \tilde{z}^4 - \frac{5 + c_1}{3} \bar{\mu}^2 \tilde{\tau}^4 \tilde{z}^2 + \mathcal{O}(\bar{\mu}^3) \\ H(\tilde{\tau}, \tilde{\eta}, \tilde{z}) &= -2\bar{\mu}^2 \tilde{\tau}^2 \tilde{z}^4 - \frac{5 + c_1}{3} \bar{\mu}^2 \tilde{\tau}^4 \tilde{z}^2 + \mathcal{O}(\bar{\mu}^3) \\ M(\tilde{\tau}, \tilde{\eta}, \tilde{z}) &= 16\bar{\mu}^2 \tilde{\tau}^2 \tilde{z}^4 + \frac{10 + 2c_1}{3} \bar{\mu}^2 \tilde{\tau}^4 \tilde{z}^2 + \mathcal{O}(\bar{\mu}^3) \end{aligned} \quad (2.3)$$

by solving Einstein's equations  $R_{\mu\nu} - \frac{1}{2}g_{\mu\nu}R - 6g_{\mu\nu} = 0$ . Here  $c_1$  is a freely choosable integration constant that corresponds to some unfixed diffeomorphism freedom. Following Refs.[8, 9], our numerical setup requires a line-element in the Eddington-Finkelstein form and, therefore, we have to transform to new coordinates  $\tau, \eta, z$ . The relation between the old and new coordinates in the small  $\bar{\mu}$  limit may be found to be

$$\begin{aligned} \tilde{\tau} &= \tau + z - \frac{\bar{\mu}}{2} z^4 \cosh[Y - \eta] - \frac{1}{2} \bar{\mu}^2 z^4 (\tau + z)^3 c_1 + \bar{\mu}^2 \cosh[2(Y - \eta)] z^6 (\tau + z) \\ &\quad - \frac{\bar{\mu}^2}{210} z^4 (175\tau^3 + 469\tau^2 z + 378\tau z^2 + 52z^3) - \frac{\bar{\mu}^2 z^8 \sinh^2[Y - \eta]}{8(\tau + z)} + \mathcal{O}(\bar{\mu}^3) \\ \tilde{\eta} &= \eta - \frac{\bar{\mu} z^4 \sinh[Y - \eta]}{2(\tau + z)} + \frac{\bar{\mu}^2 (8\tau^2 + 16z + 7z^2)}{8(\tau + z)^2} z^6 \sinh[2(Y - \eta)] + \mathcal{O}(\bar{\mu}^3) \\ \tilde{z} &= z - 2\bar{\mu} z^3 (\tau + z) \cosh[Y - \eta] - \frac{\bar{\mu}^2 z^3 (\tau + z)^4 c_1}{6} + \bar{\mu}^2 \cosh[2(Y - \eta)] 6z^5 (\tau + z)^2 \\ &\quad - \frac{\bar{\mu}^2}{30} z^3 (25\tau^4 + 100\tau^3 z + 25\tau^2 z^2 - 146\tau z^3 - 119z^4) + \mathcal{O}(\bar{\mu}^3). \end{aligned} \quad (2.4)$$

It turns out that to this order in the shock strength  $\mu$ , the metric in Eddington-Finkelstein coordinates is independent of  $\eta$  and hence boost-invariant in the sense of Bjorken [18]. Higher order corrections turn out to spoil this invariance, but it seems that — at least for weak

shocks with  $\mu \ll 1$  — the initial dynamics is predominantly boost-invariant. In Eddington-Finkelstein coordinates, the line element can be parametrized in the following form

$$ds^2 = 2drd\tau - Ad\tau^2 + \Sigma^2 e^B dx_\perp^2 + \Sigma^2 e^{-2B} d\eta^2, \quad (2.5)$$

where using  $r = \frac{1}{z}$  the metric functions are given as

$$\begin{aligned} A &= r^2 - \frac{6\bar{\mu}^2}{5r^4} - \frac{4\bar{\mu}^2\tau}{3r^3} - \frac{4\bar{\mu}^2\tau^2}{3r^2} + \mathcal{O}(\bar{\mu}^3), \\ B &= -\frac{2}{3}\log\left(\frac{1+r\tau}{r}\right) + \frac{(612 + 7r\tau(234 + r\tau(217 + 75r\tau)))\bar{\mu}^2}{315r^6(1+r\tau)} + \mathcal{O}(\bar{\mu}^3), \\ \Sigma^3 &= r^2(1+r\tau) + \frac{(72 + 14r\tau(9 + 5r\tau))\bar{\mu}^2}{105r^4} + \mathcal{O}(\bar{\mu}^3). \end{aligned} \quad (2.6)$$

### A. Einstein's equations in Eddington-Finkelstein coordinates

In Eddington-Finkelstein coordinates (2.5), Einstein's equations become [8]

$$0 = \Sigma \dot{\Sigma}' + 2\Sigma' \dot{\Sigma} - 2\Sigma^2, \quad (2.7a)$$

$$0 = \Sigma \dot{B}' + \frac{3}{2}(\Sigma' \dot{B} + B' \dot{\Sigma}), \quad (2.7b)$$

$$0 = A'' + 3B' \dot{B} - 12\Sigma' \dot{\Sigma}/\Sigma^2 + 4, \quad (2.7c)$$

$$0 = \ddot{\Sigma} + \frac{1}{2}(\dot{B}^2 \Sigma - A' \dot{\Sigma}), \quad (2.7d)$$

$$0 = \Sigma'' + \frac{1}{2}B'^2 \Sigma, \quad (2.7e)$$

where for any function  $h(r, \tau)$  we have defined

$$\dot{h} \equiv \partial_\tau h + \frac{1}{2}A \partial_r h, \quad (2.8)$$

and  $h' \equiv \partial_r h$ . Under the coordinate transformation

$$r \rightarrow \hat{r} = r - f, \quad (2.9)$$

one has

$$\hat{A} = A(\hat{r} + f, \tau) - 2\frac{df}{d\tau}, \quad \hat{\Sigma} = \Sigma(\hat{r} + f, \tau), \quad \text{and} \quad \hat{B} = B(\hat{r} + f, \tau), \quad (2.10)$$

where  $f$  is an arbitrary function of  $\tau$ . It is easy to check that Einstein's equations are form-invariant under the above diffeomorphism.

In the following, we will take (2.7d) and (2.7e) as constraint equations and numerically solve (2.7a)-(2.7c), which can be rewritten in the following form

$$\theta' = S, \tag{2.11a}$$

$$\phi' = 3B'S^{-\frac{1}{2}}\theta, \tag{2.11b}$$

$$\dot{S} = 6\theta, \tag{2.11c}$$

$$\dot{B} = -S^{-\frac{1}{2}}\phi, \tag{2.11d}$$

$$A'' = 8\theta S'S^{-2} + 3B'\phi S^{-\frac{1}{2}} - 4, \tag{2.11e}$$

where  $S \equiv \Sigma^3$ .

## B. Apparent Horizons and Area of Trapped Surface

The area of the trapped surface formed in the collision of two shock waves is of considerable interest since at late times, when the system is close to equilibrium, it can be used to extract the entropy of the system. Far from equilibrium, its physical interpretation is difficult [16] but it is nevertheless interesting to track the area spanned by the apparent horizon, which is the location where out-going null vectors vanish. It should be pointed out that the apparent horizon is a local concept, coordinate-time dependent, and not invariant under coordinate transformations (space-time slicings).

The location of apparent horizon may be calculated as follows: first determine the in and out-going null vectors  $l^-, l^+$  (corresponding to “light-rays” in ordinary space-time) from the condition  $g^{\mu\nu}l_\mu l_\nu = 0$ . Then find the apparent horizon from the criterion of vanishing expansion of the out-going null vectors,

$$h^{ab}\nabla_a l_b^+ = 0, \tag{2.12}$$

where  $h^{ab}$  is the projected metric that is given by  $h_{ab} = g_{ab} - \frac{l_a^+ l_b^- + l_a^- l_b^+}{l^+ \cdot l^-}$ . (The projected metric fulfills the requirement that multiplying  $l^+$  by an arbitrary function  $B$  does not change the result (2.12)).

### 1. Before the collision

Just before the collision of the two shock waves, where the line element is given by a superpositions of line elements of the form (2.1), the location of the apparent horizon may

be calculated along the lines of [19]: parametrizing the surface at  $u = 0$  by  $v = -\psi_1(\tilde{z})$ , the normals to this surface are given by  $du, dv + d\psi_1$ , so normal vectors  $l_\mu$  can be parametrized as  $l_\mu dx^\mu = c_1 du + c_2(dv + d\psi_1)$ . The condition  $g^{\mu\nu} l_\mu l_\nu = 0$  at  $u = 0$  leads to the conditions  $c_1 = c_2 \frac{\psi_1'^2(\tilde{z})}{2}$  or  $c_2 = 0$ , where the prime here denotes a derivative with respect to  $\tilde{z}$ . As a consequence we obtain a set of (out-going and in-going) null vectors  $l_\mu^\pm$  normal to the surface at  $u = 0$

$$l_\mu^+ = \left( \frac{\psi_1'^2(\tilde{z})}{2}, 1, \mathbf{0}_\perp, \psi_1'(\tilde{z}) \right), \quad l_\mu^- = (1, 0, \mathbf{0}_\perp, 0).$$

(The constant function multiplying these vectors is arbitrary and has been set to unity.)

Vanishing expansion implies

$$\square \left[ \psi_1(\tilde{z}) - \frac{1}{2}\phi(\tilde{z}) \right] = 0,$$

which has the solution  $\psi_1(\tilde{z}) = \frac{1}{2}\phi(\tilde{z}) + c$ , where the constant  $c$  is unimportant for the following. To obtain the location of the trapped surface  $\tilde{z} = \tilde{z}_H$ , we use the following boundary condition: we could have equally well started with the other shock wave and a surface at  $v = 0$  parametrized as  $u = -\psi_2(\tilde{z})$ . Since at  $u = v = 0$  both surface normal vectors have to coincide, one finds  $\psi_1 = \psi_2$  and  $\psi_1'^2(\tilde{z}_H) = 2 = \frac{1}{4}\phi'^2(\tilde{z}_H)$  and as a consequence

$$\tilde{z}_H = (2\bar{\mu}^2)^{-1/6}.$$

Now the ‘‘area’’ of the trapped surface is given by

$$A_h = \int \sqrt{\det g_{ab}|_S} dx_\perp d\tilde{z} = \int dx_\perp \int_{\tilde{z}_H}^\infty \frac{1}{\tilde{z}^3} d\tilde{z} = \left( \frac{\bar{\mu}}{2} \right)^{2/3} \int dx_\perp$$

where  $g_{ab}|_S$  is the induced metric on the trapped surface, which can be calculated by using  $du = 0, dv + d\psi_1(\tilde{z}) = 0$  in the line element.

## 2. After the collision for weak shocks

For the line element (2.5) we parametrize the location of the apparent horizon by  $r = r_h(\tau)$  at constant  $\tau$ , which leads to  $l_\mu dx^\mu = (c_1 - c_2 r_h') d\tau + c_2 dr$ . The conditions for null vectors are  $c_1 = -\frac{1}{2}c_2 A + c_2 r_h'$  and  $c_2 = 0$ , so that for constant  $\tau$

$$l_\mu^+ = \left( -\frac{1}{2}A, 0, 0, 0, 1 \right) \quad l_\mu^- = (1, 0, 0, 0, 0).$$

Vanishing expansion implies  $\dot{\Sigma} \equiv \partial_\tau \Sigma + \frac{1}{2}A \partial_r \Sigma = 0$ , or equivalently  $\dot{S} = 0$  where we recall that  $S \equiv \Sigma^3$ . Because of (2.11c), an equivalent condition is  $\theta(r = r_h) = 0$ , which is

sometimes easier to use because the definition of  $\theta$  does neither involve the function  $A$  nor explicit time derivatives.

Using the values for  $A, \Sigma$  from (2.6) to solve  $\dot{S}(r = r_h) = \mathcal{O}(\mu^3)$  (or equivalently integrating  $S$  to obtain  $\theta(r)$  and solving for  $\theta(r = r_h) = \mathcal{O}(\mu^3)$ ) one finds in the limit  $\tau \rightarrow 0$

$$r_h(\tau = 0) \sim \left( \frac{24\bar{\mu}^2}{35} \right)^{1/6} \quad (2.13)$$

and the horizon area becomes

$$A_h(\tau = 0) = \int dx_\perp d\eta \Sigma^3 \sim \frac{192^{1/3} \bar{\mu}^{2/3}}{35^{1/3}} V, \quad (2.14)$$

with  $V = \int dx_\perp d\eta$ .

This result is qualitatively the same as in Sec. II B 1, which is encouraging. However, there may be sizeable quantitative corrections to the above numbers, which can be traced back to the approximation used in deriving (2.6), namely small  $\mu$ . In terms of the variable  $z = 1/r$  it is apparent that while corrections  $\mathcal{O}(\mu^3)$  to (2.6) are suppressed close to the boundary  $z = 0$ , they become of order unity when  $\bar{\mu}z^3 \sim 1$ , or  $r \sim \bar{\mu}^{1/3}$ . Hence, the line element is not a valid approximation close to the apparent horizon and in particular will not fulfill Einstein's equations there. For this reason, we will make an ansatz for the line element in Eddington-Finkelstein coordinates that corresponds to (2.6) for small  $\mu$ , but is a solution to Einstein's equations everywhere.

### C. An ansatz for the post-collision line element

The ansatz we choose for the line element is to take

$$\Sigma^3 = r^2(1 + r\tau) + \frac{(72 + 14r\tau(9 + 5r\tau))\bar{\mu}^2}{105(r^4 + \bar{c}\bar{\mu}^{4/3})}, \quad (2.15)$$

where  $\bar{c}$  is a positive constant ('fudge parameter'). This ansatz agrees with the "perturbative" result (2.6) in the limit of small  $\bar{\mu}$  and/or small  $\bar{c}$ . In the scheme we will employ, the coefficient functions  $A, B$  can be calculated numerically from Einstein's equations. We are then able to study a toy model for shock wave collisions that involves one unknown number,  $\bar{c}$ .

On the CFT side, the above initial geometry corresponds to a strongly coupled gauge theory ( $\mathcal{N} = 4$  SYM) with the energy density

$$\epsilon \equiv T_{\tau\tau} = \kappa \bar{\mu}^2 \tau_0^2 + \mathcal{O}(\tau_0^3). \quad (2.16)$$



TABLE I. Smallest allowed  $\bar{c}$  at different initial times.

| $\tau_0$  | 0    | 0.1  | 0.2  | 0.3  | 0.4  | 0.5  | 1.0   |
|---|------|------|------|------|------|------|-------|
| $\bar{c}_{\min}(\tau_0)$                            | 2.88 | 3.43 | 4.10 | 4.93 | 5.97 | 7.26 | 19.84 |
| $V^{-1}\bar{\mu}^{-2/3}A_h(\tau_0, \bar{c}_{\min})$ | 0.83 | 0.92 | 1.02 | 1.15 | 1.30 | 1.47 | 2.85  |

This initial condition implies that the initial energy density does not depend on the choice for  $\bar{c}$  (nor does any other component of the CFT stress tensor).

By contrast, the area of the apparent horizon  $A_h(\tau) = S(r_h, \tau)$  depends significantly on  $\bar{c}$ . For the gauge choice  $f = 0$  (see (2.9)) and in the limit  $\tau_0 \rightarrow 0$  and  $\bar{c} \ll 1$ , the horizon position and area correspond to Eqs. (2.13) and (2.14), respectively, while for  $\bar{c} \gg 1$  they are given by  $r_h(\tau_0 \ll 1, \bar{c} \gg 1) = \left(\frac{648\pi^2\bar{\mu}^2}{1225\bar{c}^{3/2}}\right)^{1/6}$  and  $A_h(\tau_0 \ll 1, \bar{c} \gg 1) = r_h^2V$ . Since  $A_h$  is a monotonously decreasing function of  $\bar{c}$ , we may try to approximate its behaviour by the Padé inspired ansatz

$$A_h(\tau_0 \ll 1) = \bar{\mu}^{2/3}V \frac{k_0}{\sqrt{k_1 + \bar{c}}}, \quad (2.17)$$

fixing the constants  $k_0, k_1$  from the known large and small  $\bar{c}$  limits as  $k_0 = \left(\frac{648\pi^2}{1225}\right)^{1/3}$ ,  $k_1 = \left(\frac{27\pi^2}{280}\right)^{2/3}$ . We find that this ansatz gives a quite accurate approximation of the numerically determined horizon area for arbitrary  $\bar{c}$  in the limit of small  $\tau_0$ .

Unfortunately, not all values of  $\bar{c}$  lead to physically acceptable initial conditions, because (2.7e) requires that  $3S\partial_r^2S - 2(\partial_rS)^2 < 0$  for  $r > r_h$ , which is not fulfilled for any  $\bar{c}$ . Specifically,  $3S\partial_r^2S - 2(\partial_rS)^2 > 0$  for  $r > r_V$ , with  $r_V(\tau_0, \bar{c})$  a monotonously increasing function of  $\bar{c}$ . The condition  $r_V(\tau_0, \bar{c}) < r_h(\tau_0, \bar{c})$  leads to the requirement  $\bar{c}(\tau_0) > \bar{c}_{\min}(\tau_0)$ , with  $c_{\min}$  specified in Tab. I.

### III. NUMERICS

Near the boundary  $r \rightarrow \infty$ , the metric coefficient functions may be expanded in a power series of the following form

$$A = r^2 \sum_{n=0}^{\infty} \frac{a_n}{r^n}, \quad B = \sum_{n=0}^{\infty} \frac{b_n}{r^n}, \quad \Sigma = r \sum_{n=0}^{\infty} \frac{c_n}{r^n}, \quad (3.1)$$

where  $a_0 = 1$ ,  $b_0 = -\frac{2}{3} \log \tau$  and  $c_0 = \tau^{\frac{1}{3}}$ , which are determined by the boundary conditions

$$A|_{r \rightarrow \infty} = r^2, \quad B|_{r \rightarrow \infty} = -\frac{2}{3} \log \tau, \quad A|_{r \rightarrow \infty} = \tau^{\frac{1}{3}} r. \quad (3.2)$$

Specifically, to the order we will work, we use

$$\begin{aligned} A &= A_s + \tilde{A}, & B &= B_s + \tilde{B}, & \Sigma &= \Sigma_s + \tilde{\Sigma}, \\ \theta &= \theta_s + \tilde{\theta}, & \phi &= \phi_s + \tilde{\phi}, \end{aligned} \quad (3.3)$$

where the index  $s$  indicates power series expansions. There are only two series coefficients,  $a_1$  and  $a_4$ , that can not be solved from (2.7). Via holographic renormalization [20, 21], the coefficient  $a_4$  is related to the boundary stress tensor by

$$T_{\mu\nu} = -\frac{3\kappa}{4} \text{diag} \left\{ a_4, a_4 + \frac{\tau}{2} \partial_\tau a_4, a_4 + \frac{\tau}{2} \partial_\tau a_4, -\tau^2 (a_4 + \tau \partial_\tau a_4) \right\}, \quad (3.4)$$

so that we can read off the energy density, longitudinal and transverse pressure of the medium as

$$\epsilon \equiv -\frac{3\kappa a_4}{4}, \quad p_L \equiv \frac{3\kappa}{4} (a_4 + \tau \partial_\tau a_4), \quad p_T \equiv \frac{3\kappa}{4} \left( -a_4 - \frac{\tau}{2} \partial_\tau a_4 \right).$$

In contrast,  $a_1$  corresponds to the gauge redundancy in (2.9) and, therefore, does not appear in any physical quantity. In appendix A, all the series metric functions  $A_s$ ,  $B_s$ ,  $\Sigma_s$ ,  $\theta_s$  and  $\phi_s$  needed in our code are given by taking  $a_1$  and  $a_4$  as arbitrary functions of  $\tau$ . The series expansions in (3.1) with different gauge choices of  $a_1$  are also related to each other according to the transformation in (2.9) and (2.10) with  $a_1 = 2f$ .

## A. Numerical method

Einstein's equations will be solve by the pseudo-spectral method described in Ref. [22]: spectral differentiation in  $r$  and finite differences in  $\tau$ . The algorithm in the simplest gauge choice  $f = 0$  is described in details in Ref. [9]. In this case, we would need to impose lower cutoff  $L_{\min}$  for the integration domain which needs to fulfill the requirement  $L_{\min} < r_h(\tau)$  for all  $\tau$ . We found this approach to work well for late time (near-equilibrium) situations, where it is furthermore computationally cheap. However, at early times (far from equilibrium),  $r_h(\tau)$  depends strongly on  $\tau$ , and hence it is inconvenient to set up a computational domain with fixed  $L_{\min}$ . In these circumstances, one can use an alternative method. Since the inside of the horizon is causally disconnected from outside observers on the boundary, the

computational domain can be chosen to be  $r \geq r_h(\tau)$ . One can use the diffeomorphism (2.9) to fix  $r_h$  to a given value, say, unity<sup>1</sup>, in which case the only sensible choice for the cutoff becomes  $L_{\min} = 1$ . Besides the lower cutoff it is also necessary to truncate the computational domain at large radii at  $r = L_{\max}$  for numerical reasons discussed in the next subsection.

As for any pseudo-spectral method, we have to choose the location of grid points (corresponding to a choice of basis functions), called collocation points [22]. For  $N + 1$  points we choose

$$r_j = ae^{b \cos(\frac{j\pi}{N})} + c, \quad (3.5)$$

where  $a$ ,  $b$  and  $c$  are fixed by

$$r_0 = L_{\max}, \quad r_N = L_{\min}, \quad \text{and} \quad r_{N/2} = H,$$

that is,

$$a = \frac{H^2 - HL_{\max} - HL_{\min} + L_{\max}L_{\min}}{2H - L_{\max} - L_{\min}}, \quad (3.6)$$

$$b = \log\left(\frac{L_{\max} - H}{H - L_{\min}}\right), \quad (3.7)$$

$$c = -\frac{H^2 - L_{\max}L_{\min}}{L_{\max} + L_{\min} - 2H}. \quad (3.8)$$

Here,  $H$  will be chosen to ensure that our algorithm is numerically stable at a relatively large time step  $d\tau$ . In the following, we will denote a function  $f$  evaluated at any collocation point  $r_j$  by  $f_j$ . Then the derivative of the function  $f$  at  $r_i$  is given in terms of the differentiation matrix  $D_{N+1}$ ,

$$f'_i \equiv f'(r_i) = \sum_{j=0}^N D_{N+1,ij} f_j, \quad D_{N+1,ij} = \frac{e^{-b \cos(\frac{i\pi}{N})}}{ab} d_{N+1,ij}$$

where [22]

$$(d_{N+1})_{ij} = \begin{cases} \frac{2N^2+1}{6} & i = j = 0 \\ \frac{-\cos(\frac{i\pi}{N})}{2(1-\cos^2(\frac{j\pi}{N}))} & 0 < i = j < N \\ \frac{c_i}{c_j} \frac{(-1)^{i+j}}{\cos(\frac{i\pi}{N}) - \cos(\frac{j\pi}{N})} & i \neq j \\ -\frac{2N^2+1}{6} & i = j = N \end{cases} \quad (3.9)$$

---

<sup>1</sup> Careful readers will notice that the mass dimension of  $r_h$  would prohibit us to set it to unity. However, one can fix this by introducing an overall dimensionful scale in the problem that will turn out to cancel everywhere in physical observables. The definitions given below should be understood in this sense.

with  $c_0 = c_n = 2$  and  $c_j = 1$  otherwise. For the sake of numerical accuracy, if

$$f(r, \tau)|_{r \rightarrow \infty} = f_0(\tau)r^n, \quad n > 0 \quad \text{and} \quad f_0 \text{ is a function only of } \tau, \quad (3.10)$$

we, instead, calculate the derivative of  $f$  by

$$f'_i = \frac{nf_i}{r_i} + r_i^n \sum_{i=0}^N D_{N+1,ij} \frac{f_j}{r_j^n}. \quad (3.11)$$

Note that since  $D_{N+1}$  acting on a constant vector is vanishing, it contains a zero eigenvalue and hence is not invertible. For this reason, we consider an alternative version where we drop the collocation point  $j = 0$  (corresponding to  $r = L_{\max}$ , the point closest to the boundary) and define an  $N \times N$  matrix

$$\tilde{D}_{N,ij} \equiv D_{N+1,ij}, \quad i, j = 1, \dots, N. \quad (3.12)$$

Using  $\tilde{D}_N$  instead of  $D_{N+1}$ , we have to supply boundary conditions at  $r = L_{\max}$  to conserve the total number of equations.  $\tilde{D}_N$  is invertible and one can numerically solve  $\tilde{D}_N^{-1}$ , the inverse of  $\tilde{D}_N$ , once for all to save computation time.

Assuming that  $A$ ,  $B$  and  $S$  are known at  $\tau$ , one can first calculate  $\theta$  and  $\phi$  at  $\tau$  by solving (2.11a) and (2.11b) with the boundary conditions in (A5) and (A6). It is of numerical advantage to deal with the “residual” metric functions  $\tilde{\theta}$  and  $\tilde{\phi}$  defined in (3.3) instead. Using the differentiation matrices, the solutions are

$$\begin{aligned} \tilde{\theta}_j &= \sum_{i=1}^N \tilde{D}_{N,ji}^{-1} \tilde{S}_i, \\ \tilde{\phi}_j &= 3 \sum_{i=1}^N \tilde{D}_{N,ji}^{-1} \left( S_i^{-\frac{1}{2}} \theta_i \sum_{k=0}^N D_{N+1,ik} B_k - \phi'_{si} \right), \end{aligned} \quad (3.13)$$

where  $j = 1, 2, \dots, N$ ,  $\tilde{\theta}_0 = 0$  and  $\tilde{\phi}_0 = 0$ . The numerical algorithm to solve Einstein’s equations is then as follows:

1. Obtain  $a_4$ ,  $S$  and  $B$  at  $\tau + d\tau$  by solving the difference equations of (A4), (2.11c) and (2.11d). To be more specific, in our code the equations are solved using a third-order Adams-Bashforth method, that is,

$$h(\tau + d\tau) = h(\tau) + \frac{d\tau}{12} [23v(\tau) - 16v(\tau - d\tau) + 5v(\tau - 2d\tau)], \quad (3.14)$$

for a general ordinary differential equation of the form  $\frac{dh}{d\tau} = v$ .

2. Then, calculate  $b_4$  and  $a_1/r_h$  at  $\tau + d\tau$ . To do this, we use the first-order implicit Euler scheme to discretize

$$\frac{d}{d\tau}h(\tau + d\tau) = \frac{h(\tau + d\tau) - h(\tau)}{d\tau}, \quad \frac{d^2}{d\tau^2}h(\tau + d\tau) = \frac{h(\tau + d\tau) - 2h(\tau) + h(\tau - d\tau)}{d\tau^2}, \quad (3.15)$$

where  $h = a_1, b_4$ . In this paper, we use the following two algorithms corresponding to two different ways to fix the gauge function  $f = a_1/2$ .

- (a) Alg. I:  $f = 0$

In this case, one needs only to solve  $b_4$  from the discretized version of the equation  $B_{s0}|_{a_1=0} = B_0$ , and  $r_h(f = 0)$  can be calculated by  $\theta(r_h, \tau + d\tau) = 0$  after one has obtained  $\theta$  at  $\tau + d\tau$  in Step 3.

- (b) Alg. II:  $r_h(f) = 1$

In this case, one needs to solve two coupled differential equations given by  $B_{s0} = B_0$  and  $\theta_N(\tau + d\tau) \equiv \theta(1, \tau + d\tau) = 0$ . Using the discretization in (3.15), one can express  $b_4(\tau + d\tau)$  as a function of  $a_1(\tau + d\tau)$  and solve  $\theta_N(\tau + d\tau) = 0$  for  $a_1(\tau + d\tau)$  using (3.13) and (A5).

3. Next, calculate  $\theta$  and  $\phi$  at  $\tau + d\tau$  by (3.13) with the boundary conditions given by  $\theta_0 = \theta_{s0}$  and  $\phi_0 = \phi_{s0}$ , or equivalently,  $\tilde{\theta}_0 = 0$  and  $\tilde{\phi}_0 = 0$ .
4. Finally, one can calculate  $A = \tilde{A} + A_s$  at  $\tau + d\tau$  by integrating (2.11e). The boundary conditions are given by  $A_0 = A_{s0}$  and  $A'_0 = A'_{s0}$ , or equivalently,  $\tilde{A}_0 = 0$  and  $\tilde{A}'_0 = 0$ .  $D_{N+1}^2$  is not invertible either because it has two eigenvectors with eigenvalue 0. As a result, the discretized equation of (2.11e) gives us only  $N - 1$  linearly independent equations, which can be chosen as

$$\sum_{j=1}^N D_{N+1,ij}^2 \tilde{A}_j = \left( 8\theta_i S_i' S_i^{-2} + 3\phi_i S_i^{-\frac{1}{2}} \sum_{j=0}^N D_{N+1,ij} B_j \right) - 4 - A''_{si}, \quad (3.16)$$

where  $i = 2, \dots, N$  and  $S'$  is calculated from (3.11) with  $n = 3$ . One needs one more equation to solve all  $A_i$  with  $i = 1, 2, \dots, N$ , which is given by

$$\tilde{A}'_0 = \sum_{i=1}^N D_{N+1,0i} \tilde{A}_i = 0. \quad (3.17)$$

$\tilde{A}$  at  $\tau + d\tau$  can be easily obtained by solving the  $N$  linear equations (3.16),(3.17).

5. Repeating steps 1-4 one can get the geometry in the bulk at all times.

To summarize, the numerical algorithm discretizes Einstein's equations using the calculational parameters  $L_{\max}, N, d\tau$  and fixing either  $f = 0, L_{\min}$  or  $r_h(f) = 1, L_{\min} = 1$ . The continuum Einstein's equations are recovered in the limit  $L_{\max} \rightarrow \infty, N \rightarrow \infty, d\tau \rightarrow 0$ .

From the description above one can expect that the algorithm in the gauge choice  $f = 0$  (Alg. I) should be computationally cheaper than that with  $r_h(f) = 1$  (Alg. II). At late times, the location of the apparent horizon  $r_h(f = 0)$  approaches  $r = 0$ . Since  $L_{\min} < r_h$ , this implies choosing  $L_{\min} \sim 0$ . However, this can not always be done. We shall see in the next section that for some values of  $\bar{c}$  there are coordinate singularities at  $r = r_V \sim r_h$  in the initial metric set up by (2.15). In this case, one has to choose  $L_{\min} \geq r_V$  and, as a result, to stop the code when  $r_h$  falls below  $L_{\min}$ . In the following, we will use both algorithms: Alg. I for the cases  $r_V \ll r_h(\tau_0)$  and Alg. II for the cases  $r_V \sim r_h(\tau_0)$ .

## B. Code tests: late time dynamics

Let us present the performance of the above algorithms in the case where analytic results are available: the late time (hydrodynamic) behavior. In this case, the initial conditions for the code are given by the following approximate solutions in the gauge  $a_1 = 0$

$$A = r^2 + \frac{a_4}{r^2}, \quad B = -\frac{2}{3} \log \left( \tau + \frac{1}{r} \right), \quad \text{and} \quad S = \tau r^3 + r^2, \quad (3.18)$$

where  $a_4$  in the leading-order in  $\frac{1}{\tau}$  is given by  $a_4 = -\frac{w_0^4}{\tau^{4/3}}$  with  $w_0$  a constant. It should be emphasized that this initial condition is only an approximate solution to Einstein's equations, whereas in the later part of this work we will work with exact solutions as initial conditions. Here, we will investigate the time evolution of the error thus made.

Performing a full-blown numerical stability analysis of our algorithm would be interesting, but rather complicated, so we leave it for future work. However, an approximate stability criterion can be found by considering the differential operator on the left-hand side of (2.11c) and (2.11d), that is,  $\partial_\tau - \frac{1}{2}A\partial_r$ . Discretizing this operator we find

$$\frac{1}{d\tau} \left( \delta_{ij} + \frac{1}{2}d\tau O_{ij} \right), \quad O_{ij} \equiv A_i D_{N+1,ij}. \quad (3.19)$$

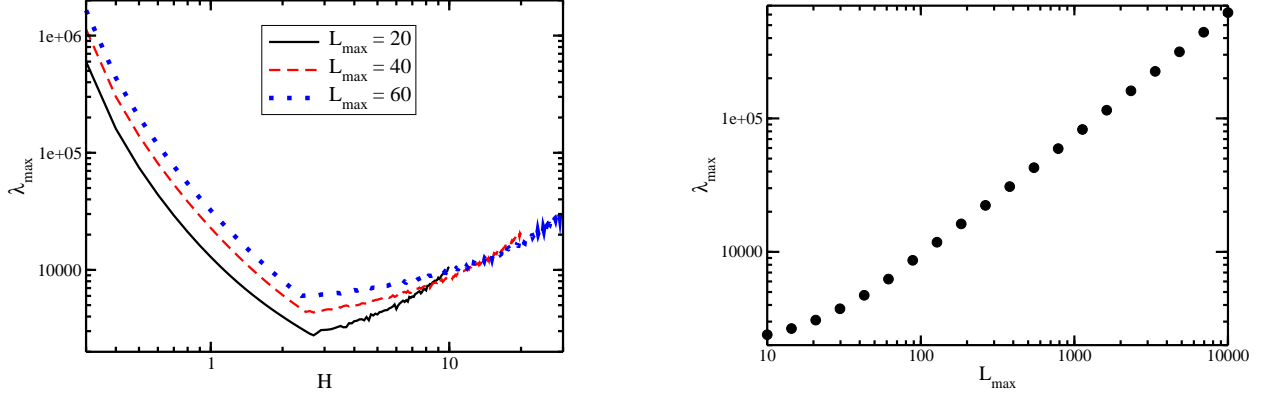


FIG. 1. The maximum eigenvalue  $\lambda_{\max}$  in Alg. I for  $N = 128$ ,  $L_{\min} = 0.2$  and  $w_0^{3/2}\tau = 4$ . Left: the dependence of  $\lambda_{\max}$  on  $H$ . For  $L_{\max} = 20, 40$  and  $60$ , the minimum  $\lambda_{\max}$  is found at  $H = 2.7, 2.7$  and  $2.6$ , respectively. Right: dependence on  $L_{\max}$  with  $H = 3.0$ .

One can argue that for the algorithm to be stable, the time increment  $\delta\tau$  has to be small enough that  $d\tau O_{ij} < \delta_{ij}$ . Estimating the size of  $O_{ij}$  by its maximum eigenvalue  $\lambda_{\max}$ , we find  $d\tau \lesssim \frac{1}{\lambda_{\max}}$ .

As shown in Fig. 1, the maximum eigenvalue  $\lambda_{\max}$  depends on the choice of the parameter  $H$  as well as  $L_{\max}$ . From this figure, one can see that the choice  $H = 3$  effectively minimizes  $\lambda_{\max}$  and hence should allow algorithmic stability for larger time increments  $d\tau$ . We adopt this choice in following. With  $\lambda_{\max} \sim 5 \times 10^3$  we therefore expect  $d\tau \lesssim 10^{-4}$  to be necessary for algorithmic stability.

In Fig. 2, we show results by Alg. I with  $d\tau = 6.1 \times 10^{-5}$  and Alg. II with  $d\tau = 6.1 \times 10^{-6}$  and  $6.1 \times 10^{-7}$ . Using Alg. II with  $d\tau = 6.1 \times 10^{-6}$ , we get numerically unstable results for the horizon position and area. However, by choosing a smaller time step, numerical stable results can also be obtained by Alg. II, which agree very well with those by Alg. I. This provides evidence for the equivalence of the two algorithms. As a rule of thumb, we find that  $d\tau = \frac{1}{N^2}$  for Alg. I and  $d\tau = \frac{10^{-2}}{N^2}$  for Alg. II generally ensures numerical stability.

For numerical reasons, it is difficult to do simulations for  $L_{\max} \gtrsim 100$ . This can be understood from Fig. 1, where it is shown that  $\lambda_{\max}$  increases exponentially with  $L_{\max}$ , forcing a similar decrease in the time increment  $d\tau$ . Also, for large  $L_{\max}$ , one confronts the subtraction of two nearly equal numbers in step 3 of the algorithm outlined in Sec. III A. Fortunately, we find in practice that for  $L_{\max} w_0^{3/2} \tau_0 \gtrsim 10$  our numerical results stabilize and

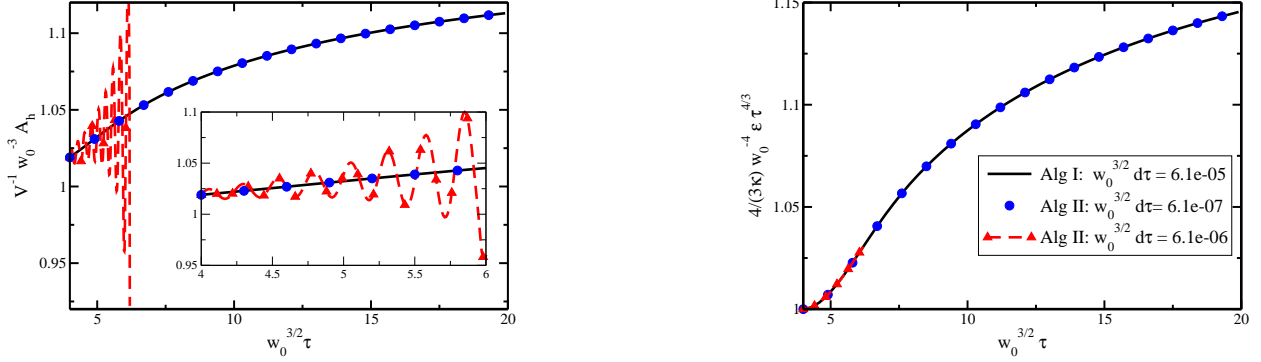


FIG. 2. Numerical stability of the two algorithms: gauge choice  $f = 0$  (denoted Alg. I) and gauge choice  $r_h(f) = 1$  (Alg. II). Shown are results for the horizon area  $A_h$  (left, inset zooms to early time behaviour), and the energy density  $\epsilon$  (right) for  $L_{max} = 20$ ,  $N = 128$  and  $H = 3.0$ . For Alg. I, results for one choice of time increment  $d\tau$  are shown (further decreasing  $d\tau$  leaves the result unchanged). In order to achieve stable results for Alg. II, we have to decrease  $d\tau$  considerably. When this is done, the results from Alg. II match those from Alg. I.

do not change appreciably when further increasing  $L_{max}$ . Thus, we are confident that the results reported in the following are close to the continuum limit  $L_{max} \rightarrow \infty$ . Conversely, note that for  $w_0^{3/2} \tau_0 \lesssim 0.1$  we would need  $L_{max} \gtrsim 100$  and therefore cannot report results for very early initial times.

We have also studied the dependence of our results on the number of collocation points  $N$ . We find that results for  $N = 64, 128, 256$  with  $d\tau = 1/N^2$  are essentially indistinguishable, while  $N = 32$  is numerically unstable for  $d\tau = 1/N^2$ , and differs on the percent level for  $d\tau = 0.1/N^2$ . Thus, we are confident that the choice  $N = 128$  is sufficiently close to the continuum  $N \rightarrow \infty$  result and shall adopt this choice in the following.

Since the initial geometry specified in Eq. (3.18) is only an approximate solution to Einstein's equations, it is important to check whether time evolution will decrease or increase the error. To answer this question quantitatively, we investigate the constraint equation (2.7e) by defining at each  $\tau$

$$\delta \equiv \max_{\{r\}} \left| \partial_r^2 \Sigma + \frac{1}{2} B'^2 \Sigma \right|, \quad (3.20)$$

where for an exact solution to Einstein's equations  $\delta = 0$ . As shown in Fig. 3,  $\delta$  initially is sizeable but decreases as a function of time until eventually stabilizing several orders of magnitude below its initial value. This implies that our algorithm approaches the exact



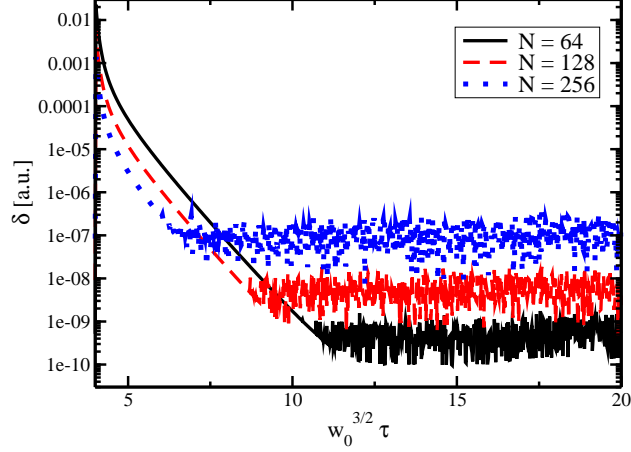


FIG. 3. Numerical error  $\delta$  in the constraint equation (2.7e) as a function of  $\tau$  for  $N = 64, 128$  and  $256$ . To test the code, we start from initial conditions that do not fulfill Einstein's equations, so  $\delta$  is initially large, but we find that in all cases  $\delta$  decreases rapidly as a function of time.

solution to Einstein's equations as time advances, rather than further deviating from it. A physical interpretation is as follows: approximate solutions satisfy Einstein's equations at large  $r$ , but not close to the horizon position  $r_h$ . However, in the particular coordinates we have chosen, the black hole acts as an absorber of the 'offending' modes, pulling them behind the horizon. As a result, the approximate solutions can quickly converge into exact solutions.

The late time hydrodynamic results for  $\epsilon$ ,  $A_h$  and  $r_h$  are given by [16]

$$\begin{aligned} \frac{4}{3\kappa}\epsilon^{\text{hydro}} &= \frac{w^4}{\tau^{4/3}} - \frac{2w^3}{3\tau^2} + \frac{1 + 2\log(2)}{18\tau^{8/3}}w^2 \\ &+ \frac{-3 + 2\pi^2 + 24\log(2) - 24\log^2(2)}{486\tau^{10/3}}w + \mathcal{O}(\tau^{-4}), \end{aligned} \quad (3.21)$$

$$\begin{aligned} V^{-1}A_h^{\text{hydro}} &= w^3 - \frac{w^2}{2\tau^{2/3}} + \frac{2 + \pi + 6\log(2)}{24\tau^{4/3}}w \\ &+ \frac{\pi^2 - 60(-1 + \log(2) + 12\log(2)^2) + 18\pi(1 + 6\log(2))}{2592\tau^2} + \mathcal{O}(\tau^{-8/3}), \end{aligned} \quad (3.22)$$

$$\begin{aligned} r_h^{\text{hydro}} &= \frac{w}{\tau^{1/3}} - \frac{1}{2\tau} + \frac{8 + 3\pi - 4\log(2)}{72w\tau^{5/3}} \\ &+ \frac{1}{w^2\tau^{7/3}} \left( \frac{\mathcal{C}}{18} + \frac{\pi w\delta_3}{3} - \frac{25\pi}{432} + \frac{1}{81} - \frac{\pi^2}{7776} + \frac{7\log^2(2)}{162} \right) \\ &- \frac{\pi\log(w)}{18} - \frac{2\log(w)}{27} - \frac{25\log(2)}{162} + \mathcal{O}(\tau^{-3}), \end{aligned} \quad (3.23)$$

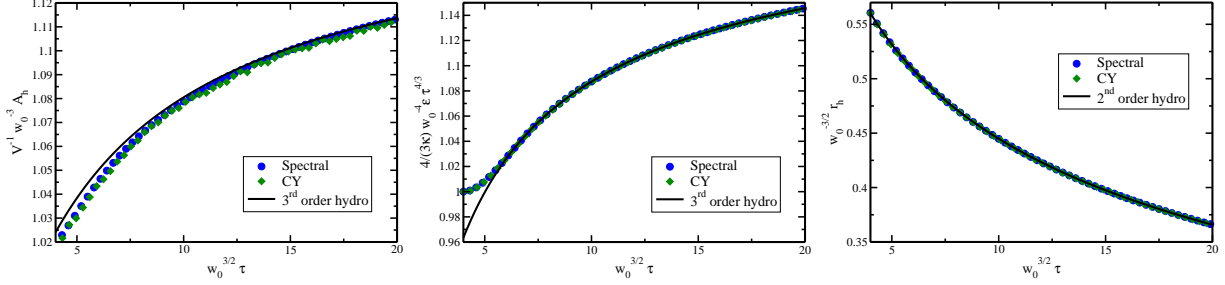


FIG. 4. Comparison of numerical results from our algorithm (“Spectral”), the algorithm from Ref. [8] (“CY”) and the  $2^{nd}/3^{rd}$  order hydrodynamics. Here, we use  $\tau_0 w_0^{3/2} = 4$ ,  $L_{max} = 20$ ,  $N = 128$ ,  $d\tau = \frac{1}{N^2}$ . Shown are  $r_h(f = 0)$  (right), energy density  $\epsilon$  (center) and apparent horizon area  $A_h$  (left). Performing a least-square fit of the numerical result for  $\epsilon$  with hydrodynamics we get  $w = 1.0573 w_0$ . The comparison between numerics and hydrodynamics for  $A_h$  and  $r_h$  (left,right) uses this value of  $w$ .

where  $r_h$  corresponds to the gauge choice  $f = 0$ <sup>2</sup> and  $\mathcal{C}$  is Catalan’s constant. To test the accuracy of our code, we show the comparison between our algorithms, the results from Ref. [8] and hydrodynamics in Fig. 4. Note that there is very good agreement between the algorithm Ref. [8] and the code used in this work. We also find that the energy density matches the  $3^{rd}$  order hydrodynamic result at  $\tau \gtrsim 6$ . We extract the parameter  $w$  governing the hydrodynamic behaviour (3.21) by performing a least-square fit to our numerical result for  $\epsilon$ . Using this value of  $w$ ,  $A_h$  matches hydrodynamics at a relatively late time while the location of the apparent horizon  $r_h$  does so at comparatively earlier times. We recall that the initial conditions we had chosen did not fulfill Einstein’s equations (see Fig.3), yet at late times, we recover hydrodynamics with the correct expansion coefficients (3.21,3.23,3.23). For exact initial conditions, we expect even better performance.

To summarize, we have extensively tested our numerical algorithm by studying the dependence of the results on the numerical parameters  $L_{max}, N, d\tau$ , suggesting that we can indeed extract results corresponding to solutions of the continuum Einstein’s equations unless starting at very early times  $\tau$ . At late times, our numerical results match the analytically known hydrodynamic behaviour as well as those from an independent code. In the following, we will now use this algorithm to numerically calculate the solution to Einstein’s equations

<sup>2</sup> There is one integral constant  $\delta_3$  in  $r_h$  which we can not fix because the  $3^{rd}$ -order hydrodynamic formula of  $A$  is still missing in the literatures.

for initial conditions modelling the collision of shock waves.

## IV. RESULTS

In this section, we study the toy model described in Sec. II C using the algorithms in the previous section. Using holography, this corresponds to a boost-invariant medium with energy density  $\epsilon(\tau_0 \ll 1) = \kappa\mu^2\tau_0^2$ . The increase of  $\epsilon$  mimics the 'contracting' stage of two nuclei passing through each other in heavy ion collisions. At late times, the system is expected to be described by hydrodynamics. Since the system expands along the longitudinal direction, one can expect that the medium has to stop contracting, and  $\epsilon$  should eventually decrease in order to match onto the hydrodynamic behaviour. Within our toy model, we are able to follow and study all stages of this evolution quantitatively in a strongly coupled  $\mathcal{N} = 4$  SYM medium.

### A. Initial conditions

Using the ansatz metric function in (2.15), we set up the initial geometry at time  $\tau = \tau_0$  by the steps given below. *Note that — unlike the test case considered in the previous section — the resulting initial condition is an exact solution to Einstein's equations.*

1. Initialize  $a_4$ . Near the boundary  $r \rightarrow \infty$ , the power series expansion of our ansatz metric function  $\Sigma$  in (2.15) is the same as that of  $\Sigma$  in (2.6) up to  $\mathcal{O}(\frac{1}{r^7})$ . Therefore,  $a_4$  must be given by the same expression as that of the approximate solutions in (2.6), that is,  $a_4(\tau_0) = -\frac{4\bar{\mu}^2\tau_0^2}{3}$ .
2. Then, initialize  $a_1(\tau_0)$ ,  $a_1(\tau_0 - d\tau)$  and  $a_1(\tau_0 - 2d\tau)$ . Inserting the ansatz in (2.15) into

(2.11a), we can solve  $\theta$  analytically in the gauge  $f = \frac{a_1}{2} = 0$ ,

$$\begin{aligned} \theta = & \frac{r^3}{3} + \frac{r^4\tau}{4} - \frac{\mu\pi(36 + 35\sqrt{\bar{c}}\bar{\mu}^{5/3}\tau^2)}{105\sqrt{2}\bar{c}^{3/4}} \\ & - \frac{\bar{\mu}(36\sqrt{2} + 7\bar{c}^{1/4}\bar{\mu}^{1/3}\tau(18 + 5\sqrt{2}\bar{c}^{1/4}\bar{\mu}^{1/3}\tau))}{210\bar{c}^{3/4}} \arctan \left[ 1 - \frac{\sqrt{2}r}{\bar{c}^{1/4}\bar{\mu}^{1/3}} \right] \\ & + \frac{\bar{\mu}(36\sqrt{2} + 7\bar{c}^{1/4}\bar{\mu}^{1/3}\tau(-18 + 5\sqrt{2}\bar{c}^{1/4}\bar{\mu}^{1/3}\tau))}{210\bar{c}^{3/4}} \arctan \left[ 1 + \frac{\sqrt{2}r}{\bar{c}^{1/4}\bar{\mu}^{1/3}} \right] \\ & + \frac{\sqrt{2}\bar{\mu}(-36 + 35\sqrt{\bar{c}}\bar{\mu}^{2/3}\tau^2)}{420\bar{c}^{3/4}} \left( \log \left[ \frac{\sqrt{\bar{c}}\bar{\mu}^{2/3} + r^2 - \sqrt{2}\bar{c}^{1/4}\bar{\mu}^{1/3}r}{\sqrt{\bar{c}}\bar{\mu}^{2/3} + r^2 + \sqrt{2}\bar{c}^{1/4}\bar{\mu}^{1/3}r} \right] \right). \end{aligned} \quad (4.1)$$

Under the transformation (2.9) with  $f = a_1/2$  we get  $\theta(f)$  and therefore can obtain  $a_1$  by solving  $\theta = 0$ . In Alg. I, one can skip this step.

3. Next, initialize  $b_4(\tau_0)$ ,  $b_4(\tau_0 - d\tau)$  and  $b_4(\tau_0 - 2d\tau)$ . As for  $a_4$ , one can get  $b_4$  from the power series expansion of  $B$  in (2.6). In this way, we have

$$b_4 = \frac{2 + 20\bar{\mu}^2\tau^6 + \tau a_1(4 + \tau a_1(3 + \tau a_1))}{12\tau^4}. \quad (4.2)$$

4. Initialize  $B(\tau)$  by integrating (2.7e) with boundary conditions given by (2.6).
5. Finally, obtain  $\theta(\tau_0)$ ,  $\phi(\tau_0)$  by (3.13) and  $A(\tau_0)$  by solving the linear equations in (3.16) and (3.17).

To use the third-order Adams-Bashforth method we also calculate the metric functions at  $\tau_0 - d\tau$  and  $\tau_0 - 2d\tau$  by repeating all the steps above.

As explained in the previous section, it is not possible to choose  $\bar{\mu}^{1/3}\tau_0 = 0$  for numerical reasons. However, since the initial conditions become less and less reliable for larger  $\tau_0$ , we want to choose  $\bar{\mu}^{1/3}\tau_0$  as small as possible such that the numerical algorithm can still be applied. The smallest value we achieved in practice was  $\bar{\mu}^{1/3}\tau_0 = 0.2$ .

## B. Transition to hydrodynamic behaviour

The initial conditions we consider do not exhibit hydrodynamic behaviour at early times. This can be clearly seen from the time dependence of the energy density, Eq.(2.16), which is very different from the hydrodynamic  $\tau^{-4/3}$  result. To study the transition from the early

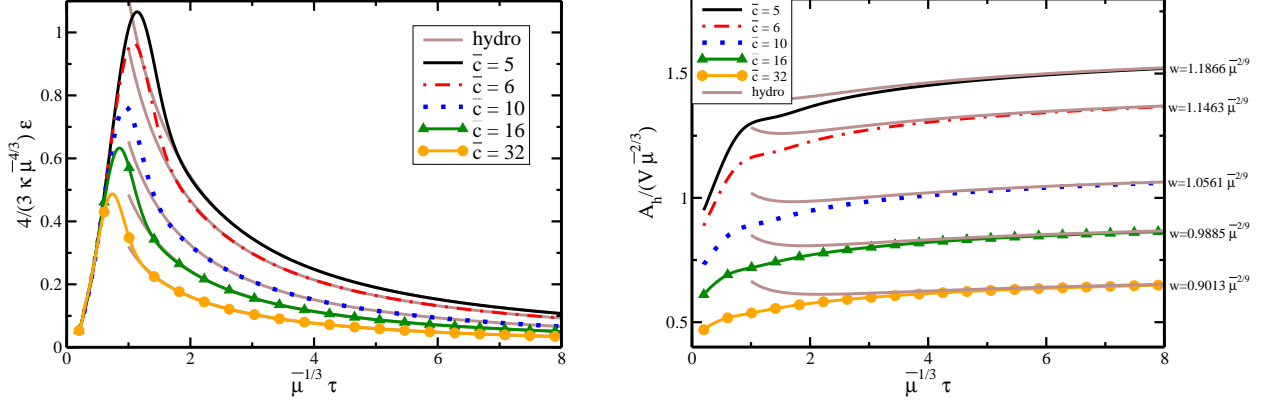


FIG. 5. The  $\tau$ -evolution of the energy density and horizon area for  $\tau_0 \bar{\mu}^{1/3} = 0.2$  and different values of  $\bar{c}$ . Lines labelled 'hydro' represent  $3^{rd}$  order hydrodynamic results. The  $w$  values indicated are obtained from hydrodynamic fits to  $\epsilon$ .

time behaviour to hydrodynamics, we choose particular values for  $\tau_0$ ,  $\bar{c}$  and then evolve the initial conditions in Sec. IV A forward in time using our numerical algorithm.

In Fig. 5, the apparent horizon area and energy density are shown for initial conditions with  $\bar{\mu}^{1/3} \tau_0 = 0.2$  and various values of  $\bar{c}$ . As can be seen from this figure, the energy density first increases, reaches a maximum at around  $\bar{\mu}^{1/3} \tau_0 \simeq 1$ , and then starts to decrease. One expects the late time dynamics to be described by hydrodynamics, Eq.(3.21). We perform a hydrodynamic least-square fit to our results for  $\epsilon$  to extract the parameter  $w$  at times<sup>3</sup>  $\bar{\mu}^{1/3} \tau > 7.5$ . The hydrodynamic results are shown together with the full numerical results in Fig. 5. As can be seen, the numerical late-time behaviour of both the energy density as well as the horizon area (using the same  $w$  values) are very well described by hydrodynamics for all chosen values of  $\bar{c}$ . One should note that the energy density is initially independent of  $\bar{c}$ , but its late time behaviour differs for different  $\bar{c}$ . This indicates that after some pre-equilibrium stage, the system indeed thermalizes, with the overall scale  $w$  dependent on the non-equilibrium initial conditions.

The behaviour of the pressure anisotropy is shown in Fig. 6, which for our initial conditions is  $p_L/p_T = -\frac{3}{2}$  at  $\tau = 0$ . One observes that while the system does not exhibit perfect isotropy (defined by  $p_T = p_L$ ) for the time extent shown, the pressure anisotropy matches the (viscous) hydrodynamic result at around  $\bar{\mu}^{1/3} \tau \sim 3$ . For all practical purposes, the sys-

<sup>3</sup> We have checked that the extracted values for  $w$  change by less than 0.0011% if we perform the fit for  $\bar{\mu}^{1/3} \tau > 6$ , indicating the insensitivity of the extracted  $w$  values.

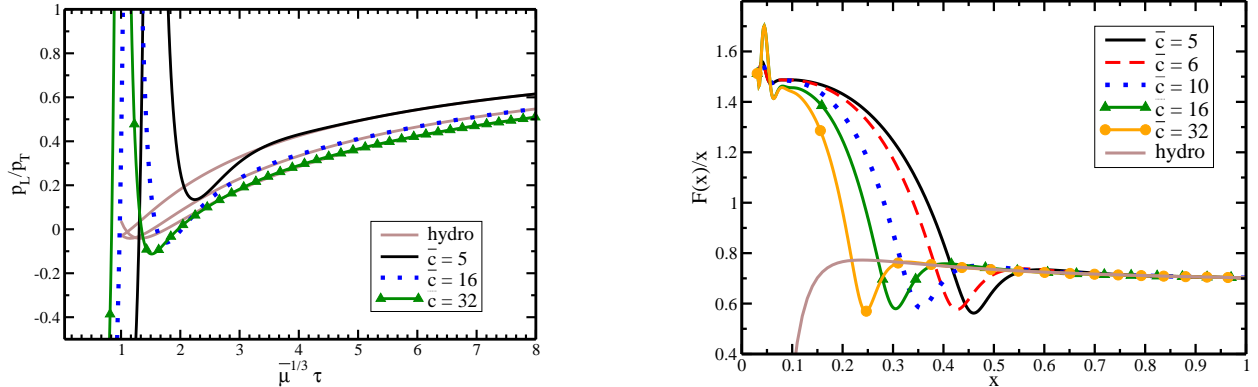


FIG. 6. Left: The  $\tau$ -evolution of the pressure anisotropy,  $p_L/p_T$  for  $\tau_0\bar{\mu}^{1/3} = 0.2$  and various values of  $\bar{c}$ . Right: The function  $F(x)/x$  for  $\tau_0\bar{\mu}^{1/3} = 0.2$  and various values of  $\bar{c}$ . In both the figures, the light grey lines are the 3<sup>rd</sup> order hydrodynamic results (hydro).

tem may therefore be regarded as 'in-equilibrium' for all times thereafter. Conversely, there does not seem to be a unique value of  $p_L/p_T$  above which hydrodynamics is applicable.

We are also able to directly compare our results with those reported in Ref. [11]. Following [11], we introduce the quantity  $\frac{F(x)}{x} = \frac{d \ln x}{d \ln \tau}$  for  $x \equiv \frac{\tau}{\pi}(-a_4)^{1/4}$ . which is known within 3<sup>rd</sup> order hydrodynamics (3.21)

$$\frac{F_{hydro}(x)}{x} = \frac{2}{3} + \frac{1}{9\pi x} + \frac{1 - \log 2}{27\pi^2 x^2} + \frac{15 - 2\pi^2 - 45 \log 2 + 24 \log^2 2}{927\pi^3 x^3}. \quad (4.3)$$

As shown in Fig. 6, our numerical results track the 3<sup>rd</sup>-order hydrodynamics solution for  $x > 0.65$ . This finding is consistent with the result reported in Ref. [11] for rather different initial conditions.

### C. Area scaling and analytic approximations

While it is numerically hard to send  $\tau_0\bar{\mu}^{1/3} \rightarrow 0$ , one can hope to learn about the early time behaviour by studying generic values of  $\tau_0$ . We thus repeat the above calculations for  $\bar{c} = 16$  for different  $\tau_0$ , always finding that the late time behaviour is well described by hydrodynamics with a parameter  $w$  depending on  $\tau_0, \bar{c}$ , that is  $w(\tau_0, \bar{c})$ . Extracting  $w(\tau_0, \bar{c})$  by a hydrodynamic fit to the energy density, we may rescale results for  $\epsilon$  and  $A_h$  using this quantity so that the late time behaviour becomes universal. The resulting curves are shown in Fig. 7.

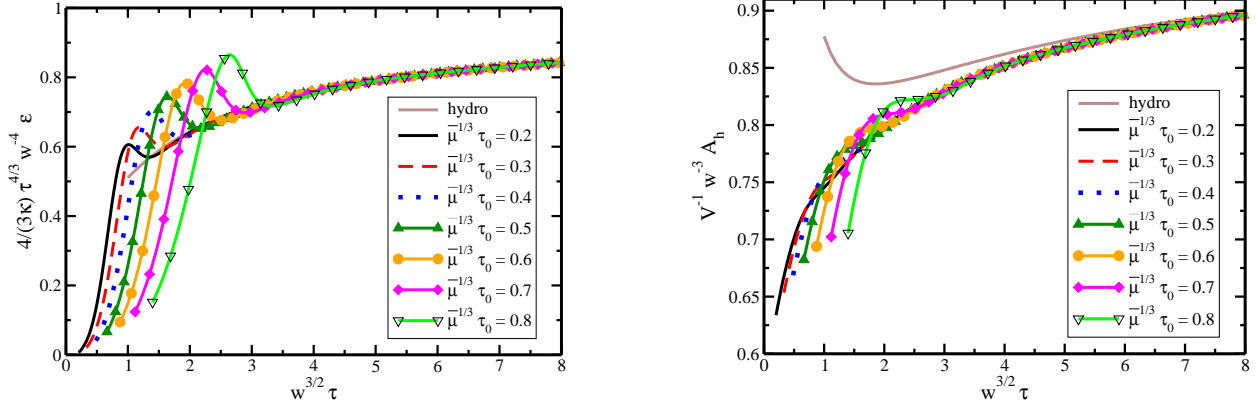


FIG. 7. The dependence of our numerical results on  $\tau_0$  with  $\bar{c} = 16$ . Shown are the energy density (left) and horizon area (right), scaled by the (fitted) parameter  $w(\tau_0, \bar{c})$  so that the late time behaviour is universal.

In Fig. 8 we plot the extracted values for  $w(\tau_0, \bar{c})$  as a function of  $\tau_0$ . Performing simple polynomial fits with degree 2 – 6 we can extrapolate to  $\tau_0 \rightarrow 0$ , finding the value  $w(0, \bar{c} = 16) = 0.885 \pm 0.02 \bar{\mu}^{2/9}$ . This suggests that we may try to obtain an analytical approximation to the time dependence of the horizon area  $A_h$  as follows: since at  $\tau_0 \rightarrow 0$  the horizon area is given by Eq. (2.17), we find  $V^{-1} A_h(\tau_0 = 0, \bar{c} = 16) / w(0, \bar{c} = 16)^3 \simeq 0.61 \pm 0.04$ . This certainly seems consistent with Fig. 7. Now knowing the late time behaviour of  $A_h$  from hydrodynamics and the initial value from Eq.(2.17), we may try to interpolate between these two using the ansatz

$$V^{-1} A_h(\tau, \bar{c}) / w^3 = \frac{u_0 + u_1 w(\bar{c}) \tau^{2/3}}{1 + d_1 w(\bar{c}) \tau^{2/3}} \quad (4.4)$$

where we can fix  $u_0, u_1, d_1$  by matching the known late and early time behaviour. We find  $u_1 = d_1$ ,  $d_1 = \frac{3}{2}(1 - u_0)$ ,  $u_0(\bar{c} = 16) = 0.61 \pm 0.04$ . The resulting time dependence is close to the one found in Fig. 7, although it could be further improved by taking into account the known higher order hydrodynamic coefficients. How does the ansatz (4.4) perform for different values of  $\bar{c}$ ? To this end, let us simply assume that  $u_0 = 0.61 \pm 0.04$  for *all* values of  $\bar{c}$ , that is, the behaviour of the horizon area Eq. (4.4) would be a universal function. In this case, it is easy to predict the value of  $w$  from inverting Eq. (4.4) as

$$w(\bar{c}, \tau_0 = 0) = \left( \frac{V^{-1} A_h(\tau_0 = 0, \bar{c})}{0.61 \pm 0.04} \right)^{1/3} \quad (4.5)$$

where  $A_h(\tau_0 = 0)$  is given by Eq. (2.17). Since we do not have direct access to  $w(\bar{c}, \tau_0 = 0)$ , we

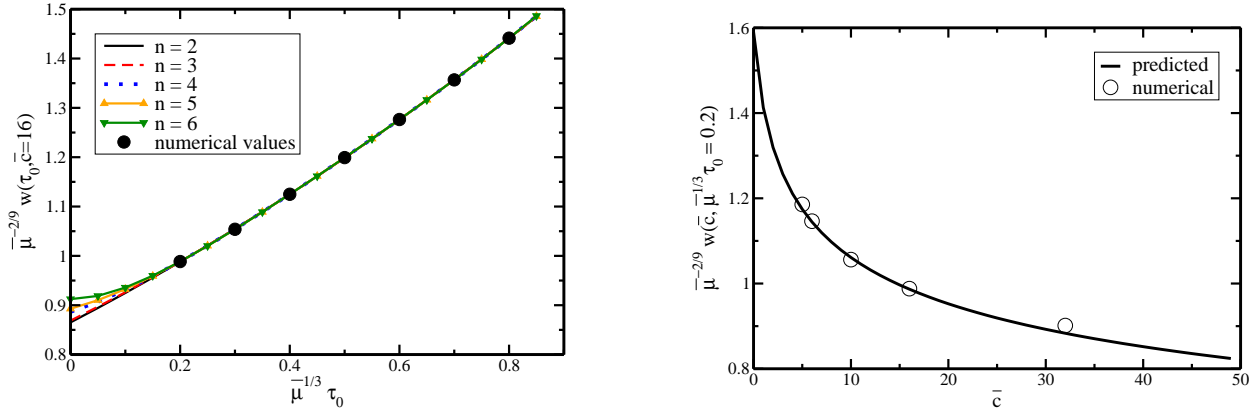


FIG. 8. Left: fitted numerical values for  $w(\tau_0, \bar{c})$  as a function of  $\tau_0$  for  $\bar{c} = 16$  and polynomial fit of degree  $n = 2, 3, 4, 5, 6$  to the  $\tau_0$  dependence. Right: extracted numerical values of  $w(\tau_0, \bar{c})$  ('numerical') vs. universal prediction (4.5).

furthermore assume that for all values of  $\bar{c}$ , the ratio  $w(\bar{c}, \tau_0 = 0.2)/w(\bar{c}, \tau_0 = 0) = \frac{0.988}{0.885 \pm 0.02}$ , i.e., the same as for  $\bar{c} = 16$ . In Fig. 8 we then compare the predicted universal values for  $w(\bar{c}, \bar{\mu}^{1/3} \tau_0 = 0.2)$  to the values extracted from our numerical simulations. Surprisingly, the predictions from the 'pocket formula' (4.5) turn out to describe the numerical values almost perfectly! Thus it seems that — at least within the class of initial conditions we consider — the late time hydrodynamic behaviour is to very good approximation determined by the area of the black hole horizon at initial times.

## V. A TOY MODEL FOR THE EARLY TIME EVOLUTION AT RHIC/LHC

In the preceding sections, we have presented numerical solutions for the time evolution of energy density and pressure in a strongly coupled medium that is expanding longitudinally in a boost-invariant manner. The initial conditions were chosen such as to mimic those following the collision of two shock waves with transverse energy density  $\mu$  given in Eq. (1.1), where we additionally introduced a 'fudge parameter'  $\bar{c}$  that (together with  $\mu$ ) determined the area of the trapped surface at  $\tau_0 = 0$ . One may now ask how well these numerical results correspond to the experimental situation for heavy-ion collisions encountered at RHIC and the LHC. Using  $a = 196, 207$  and  $R = 6.4, 6.6$  fm for the atomic number and nuclear radius of Au and Pb and  $\sqrt{s_{NN}} = 200, 2760$  GeV for the collision energies at RHIC and the LHC



we have  $\mu_{RHIC} \simeq 5.9 \text{ GeV}^3$ ,  $\mu_{LHC} \simeq 81 \text{ GeV}^3$ . Using our result Eq. (4.5) that relates the late time behaviour of the trapped surface to that at early times we can calculate the entropy density  $s \equiv \frac{\kappa\pi}{\tau V} A_h$  at 'late' times where hydrodynamics applies as

$$s \simeq \frac{2.84\pi\mu^{2/3}\kappa^{1/3}}{\tau\sqrt{0.97 + \bar{c}}}.$$

In order to interpret this as QCD entropy density at  $\tau = 1 \text{ fm}/c$ , we first need to fix the constant  $\kappa$  that is related to the number of degrees of freedom we are simulating. At late times Eqns. (3.21,3.23) correspond to  $s = \kappa\pi^4 T^3$  with  $T = \frac{w}{\pi\tau^{1/3}}$ . Since it is known that this entropy density corresponds to three quarters that of the free case, and knowing that  $s_{QCD}^{\text{free}} = \frac{4(N_c^2-1)+7N_cN_f}{45}\pi^2 T^3$  we find that we need to set

$$\kappa = \frac{4(N_c^2 - 1) + 7N_cN_f}{60\pi^2}$$

or  $\kappa \simeq 0.16$  for  $N_c = N_f = 3$  in order to model QCD. The corresponding temperatures for  $\bar{c} \rightarrow 0$  are then  $T(\tau = 1 \text{ fm}/c) \sim 0.6, 1 \text{ GeV}$  for RHIC and LHC energies, which are much too large. We may reduce the temperatures to be more in line with values used in actual hydrodynamic simulations for RHIC and the LHC (see e.g. Refs. [23–26]) by using the fudge parameter  $\bar{c}$ . Additionally, since we are limited to  $\tau_0 > 0.2\bar{\mu}^{1/3}$  one has to rescale the entropy density by a factor of order one (see preceding section). In practice, therefore, we choose  $\bar{c} = 64$  (RHIC) and  $\bar{c} = 512$  (LHC) which with the measured values of  $w\bar{\mu}^{-2/9} = 0.8264, 0.6587$  give  $T(\tau = 1 \text{ fm}/c) \sim 0.33, 0.41 \text{ GeV}$  for RHIC and LHC, respectively. With these parameters, we have a crude, yet fully dynamic model for the bulk evolution of the medium created in heavy-ion collisions from  $\tau = 0$  to the time when hydrodynamics becomes applicable. As an example, the evolution of the energy density and pressure anisotropy together with the hydrodynamic results are shown in Fig. 9. Note that from the pressure anisotropy it seems that hydrodynamics becomes applicable at around  $0.15 \text{ fm}/c$ , regardless of the collision energy. A possible application of our result would be a calculation of the non-equilibrium photon/dilepton production along the lines of Refs. [28–30] or Upsilon suppression [27], which we leave for future work.

## VI. CONCLUSIONS

In this work, we have provided numerical solutions to a boost-invariant (toy) model of shock wave collisions in  $AdS_5$ , which could be relevant to the problem of heavy-ion collisions

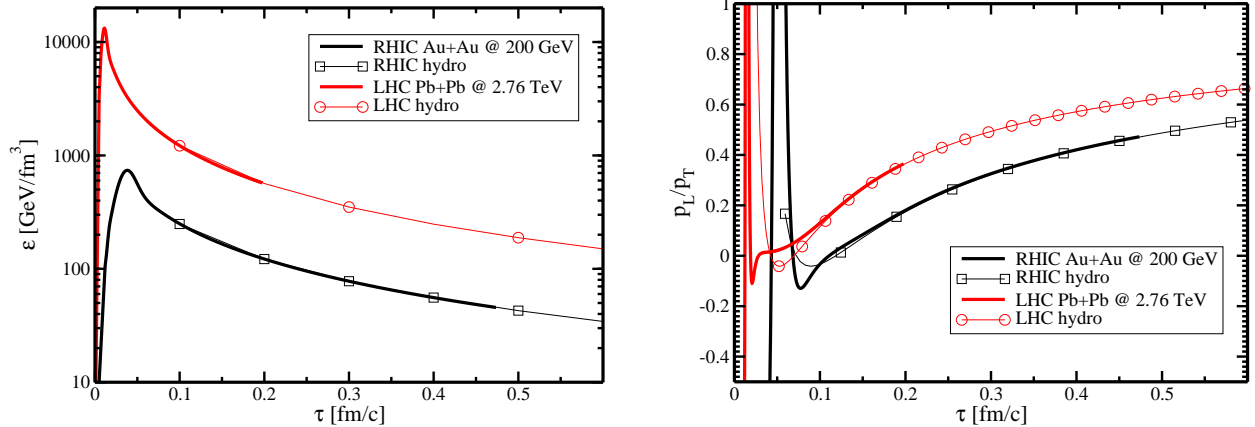


FIG. 9. Time evolution of the energy density (left) and pressure anisotropy (right) for RHIC and LHC energies, respectively.

through the AdS/CFT correspondence. Our initial conditions are such that the initial energy density evolution is given by the early time analytic solution from Ref. [3], whereas the early time horizon area is controlled by a fudge parameter. Our numerical results indicate that the late time energy density behaviour is given by hydrodynamics with a scale parameter that is determined by the initial black hole horizon area. More work is needed to decide whether this is an artefact of the class of initial conditions we consider or holds true in general. Retuning the number of degrees of freedom to make our equation of state QCD-like, and freely choosing the fudge parameter we introduced, we are able to provide dynamic models for the early time evolution of the bulk medium following heavy-ion collisions at RHIC and the LHC, including thermalization of the system. Our results may be useful for applications such as calculating non-equilibrium photon/dilepton production and are available upon request.

## ACKNOWLEDGEMENTS

We are indebted to P. Chesler for providing us with the numerical code used in Ref. [8] and we would like to thank P. Chesler, M. Martinez, M. Strickland and Zhe Xu for useful discussions. This work was supported in part by the Helmholtz International Center for FAIR within the framework of the LOEWE program launched by the state of Hesse.

## Appendix A: Near-boundary behavior of metric coefficient functions

In this paper, we need to know the following power series expansions of the metric functions near the boundary  $r \rightarrow \infty$

$$\begin{aligned}
A_s = & r^2 + a_1 r + \frac{1}{4} (a_1^2 - 4a_1') + \frac{a_4}{r^2} + \frac{2 + 3\tau^2 a_1^2 + \tau^3 a_1^3 + \tau a_1 (4 - 9\tau^4 a_4) - 6\tau^4 (a_4 + 2b_4)}{9\tau^5 r^3} \\
& + \frac{1}{60\tau^6 r^4} \left( -32 + \tau (-37\tau^2 a_1^3 - 10\tau^3 a_1^4 + 6a_1 (-12 + 10\tau^4 (a_4 + 2b_4) + 3\tau^2 a_1') + \tau a_1^2 \right. \\
& \times (-70 + 45\tau^4 a_4 + 9\tau^2 a_1') + 12\tau (a_1' + \tau^2 (2a_4 + 4b_4 - 3\tau b_4')) \left. \right) + \frac{1}{2430\tau^7 r^5} (2512 \\
& + \tau (1782\tau^3 a_1^4 + 405\tau^4 a_1^5 + \tau^2 a_1^3 (4289 - 243 (5\tau^4 a_4 + 3\tau^2 a_1'))) - 3\tau a_1^2 (-2162 + 15\tau^2 \\
& \times (54\tau^2 (a_4 + 2b_4) + 43a_1' - 3\tau a_1'')) + 2a_1 (2950 + 9\tau^2 (-137a_1' + 3\tau (\tau (-36a_4 - 72b_4 \\
& + 5a_1'^2 + 54\tau b_4') + 5a_1''))) - 6\tau (226a_1' + \tau (-30a_1'' + \tau (80a_4 + 160b_4 - 45a_1'^2 - 138\tau b_4' \\
& + 90\tau^2 b_4''))) \left. \right), \tag{A1}
\end{aligned}$$

$$\begin{aligned}
B_s = & -\frac{2 \log \tau}{3} - \frac{2}{3\tau r} + \frac{1 + \tau a_1}{3\tau^2 r^2} - \frac{4 + 3\tau a_1 (2 + \tau a_1)}{18\tau^3 r^3} + \frac{b_4}{r^4} + \frac{1}{120\tau^5 r^5} (64 + \tau (50\tau^2 a_1^3 \\
& + 15\tau^3 a_1^4 + 10\tau a_1^2 (10 - 3\tau^2 a_1') - 60a_1 (-2 + 4\tau^4 b_4 + \tau^2 a_1') + 8 (2\tau^3 a_4 - 5\tau a_1' \\
& + 15\tau^4 b_4')) + \frac{1}{2160\tau^6 r^6} (-3712 + \tau (-1575\tau^3 a_1^4 - 405\tau^4 a_1^5 + \tau^2 a_1^3 (-4031 + 1350\tau^2 a_1') \\
& + a_1^2 (-7008\tau + 45\tau^3 (120\tau^2 b_4 + 73a_1' - 7\tau a_1''))) - 2a_1 (3742 + 45\tau^2 (-47a_1' \\
& + \tau (\tau (8a_4 + 7a_1'^2 + 60\tau b_4') + 7a_1''))) + 6\tau (410a_1' + \tau (-70a_1'' + \tau (-112a_4 \\
& - 128b_4 + 15 (-7a_1'^2 + 2\tau (b_4' + 7\tau b_4'')))) \left. \right), \tag{A2}
\end{aligned}$$

and

$$\Sigma_s = \tau^{1/3} r + \frac{2 + 3\tau a_1}{6\tau^{2/3}} - \frac{1}{9\tau^{5/3} r} + \frac{10 + 9\tau a_1}{162\tau^{8/3} r^2} + \frac{-40 - 3\tau a_1 (20 + 9\tau a_1)}{972\tau^{11/3} r^3} + \mathcal{O}\left(\frac{1}{r^4}\right), \tag{A3}$$

where  $a_1$ ,  $a_4$  and  $b_4$  are functions only of  $\tau$ , which satisfy the following equation

$$a_4' = -\frac{2(-2 - 4\tau a_1 - 3\tau^2 a_1^2 - \tau^3 a_1^3 + 6\tau^4 a_4 + 12\tau^4 b_4)}{9\tau^5}. \tag{A4}$$

From Eqns. (2.11c) and (2.11d), one can also get

$$\begin{aligned}
\theta_s = & \frac{\tau r^4}{4} + \frac{1}{6}(2 + 3\tau a_1)r^3 + \frac{1}{8}a_1(4 + 3\tau a_1)r^2 + \frac{1}{8}a_1^2(2 + \tau a_1)r + \left( \frac{1}{192}a_1^3(8 + 3\tau a_1) + \frac{1}{4}\tau a_4 \right) \\
& + \frac{2 + \tau a_1(4 + \tau a_1(3 + \tau a_1)) - 12\tau^4 b_4}{30\tau^4 r} + \frac{1}{1080\tau^5 r^2} (-65\tau^3 a_1^3 - 18\tau^4 a_1^4 + 15\tau^2 a_1^2 (-10 + 3\tau^2 a_1') \\
& + a_1 (-200\tau + 216\tau^5 b_4 + 90\tau^3 a_1') - 4 (28 + 3\tau^2 (-5a_1' + \tau^2 (2a_4 + 4b_4 + 15\tau b_4')))) \\
& + \frac{1}{68040\tau^6 r^3} (10672 + \tau (2394\tau^3 a_1^4 + 567\tau^4 a_1^5 + 7\tau^2 a_1^3 (1049 - 405\tau^2 a_1') \\
& + 3\tau a_1^2 (5078 - 3\tau^2 (785a_1' + 21\tau (36\tau b_4 - 5a_1'')))) \\
& + 2a_1 (9490 + 9\tau^2 (-575a_1' + 21\tau (\tau (4a_4 + 8b_4 + 5a_1'^2 + 30\tau b_4') + 5a_1'')) - 6\tau (1150a_1' \\
& + \tau (-210a_1'' + \tau (-304a_4 - 608b_4 - 315a_1'^2 + 330\tau b_4' + 630\tau^2 b_4'')))) , \tag{A5}
\end{aligned}$$

and

$$\begin{aligned}
\phi_s = & \frac{r^{3/2}}{3\sqrt{\tau}} + \frac{(-2 + 3\tau a_1)\sqrt{r}}{12\tau^{3/2}} + \frac{(12 + \tau a_1(-4 + 3\tau a_1))\sqrt{\frac{1}{r}}}{96\tau^{5/2}} \\
& + \frac{(-168 - \tau a_1(268 + 5\tau a_1(38 + 13\tau a_1)) + 768\tau^4 b_4) \left(\frac{1}{r}\right)^{3/2}}{384\tau^{7/2}} \\
& + \frac{1}{6144\tau^{9/2}} (5680 + \tau (2552\tau^2 a_1^3 + 771\tau^3 a_1^4 + 24\tau a_1^2 (259 - 96\tau^2 a_1') \\
& - 32a_1 (-287 + 144\tau^2 (2\tau^2 b_4 + a_1')) + 3072 (2\tau^3 b_4 - \tau a_1' + 3\tau^4 b_4')) \left(\frac{1}{r}\right)^{5/2} \\
& + \frac{1}{122880\tau^{11/2}} (-226144 + \tau (-35150\tau^3 a_1^4 - 9615\tau^4 a_1^5 + 8\tau^2 a_1^3 (-14539 + 7200\tau^2 a_1') \\
& + 16\tau a_1^2 (-16711 + 480\tau^2 (15\tau^2 b_4 + 17a_1' - 3\tau a_1'')) - 16a_1 (23083 + 960\tau^2 \\
& \times (-13a_1' + \tau (10\tau b_4 + 3 (\tau (a_1'^2 + 5\tau b_4') + a_1'')))) + 1024\tau (140a_1' \\
& + \tau (-30a_1'' + \tau (-8a_4 - 54b_4 - 45a_1'^2 + 120\tau b_4' + 90\tau^2 b_4'')))) \left(\frac{1}{r}\right)^{7/2} . \tag{A6}
\end{aligned}$$

- 
- [1] J. M. Maldacena, Adv. Theor. Math. Phys. **2**, 231-252 (1998). [hep-th/9711200].
- [2] E. Witten, Adv. Theor. Math. Phys. **2**, 253-291 (1998). [hep-th/9802150].
- [3] D. Grumiller, P. Romatschke, JHEP **0808** (2008) 027. [arXiv:0803.3226].
- [4] L. Alvarez-Gaume, C. Gomez, A. Sabio Vera, A. Tavanfar, M. A. Vazquez-Mozo, JHEP **0902** (2009) 009. [arXiv:0811.3969].
- [5] S. Lin, E. Shuryak, Phys. Rev. **D79** (2009) 124015. [arXiv:0902.1508].
- [6] J. L. Albacete, Y. V. Kovchegov, A. Taliotis, JHEP **0905** (2009) 060. [arXiv:0902.3046].

- [7] K. A. Khan, R. Penrose, *Nature* **229**, 185-186 (1971).
- [8] P. M. Chesler, L. G. Yaffe, *Phys. Rev. Lett.* **102**, 211601 (2009), [arXiv:0812.2053]
- [9] P. M. Chesler, L. G. Yaffe, *Phys. Rev.* **D82**, 026006 (2010). [arXiv:0906.4426].
- [10] P. M. Chesler, L. G. Yaffe, *Phys. Rev. Lett.* **106**, 021601 (2011). [arXiv:1011.3562].
- [11] M. P. Heller, R. A. Janik, P. Witaszczyk, [arXiv:1103.3452].
- [12] S. Bhattacharyya, S. Minwalla, *JHEP* **0909** (2009) 034. [arXiv:0904.0464].
- [13] R. A. Janik, R. B. Peschanski, *Phys. Rev.* **D73**, 045013 (2006). [hep-th/0512162].
- [14] R. A. Janik, R. B. Peschanski, *Phys. Rev.* **D74**, 046007 (2006). [hep-th/0606149].
- [15] S. Kinoshita, S. Mukohyama, S. Nakamura and K. y. Oda, *Prog. Theor. Phys.* **121**, 121 (2009) [arXiv:0807.3797].
- [16] I. Booth, M. P. Heller, M. Spalinski, *Phys. Rev.* **D80**, 126013 (2009). [arXiv:0910.0748].
- [17] G. Beuf, M. P. Heller, R. A. Janik, R. Peschanski, *JHEP* **0910** (2009) 043. [arXiv:0906.4423].
- [18] J. D. Bjorken, *Phys. Rev.* **D27**, 140-151 (1983).
- [19] S. S. Gubser, S. S. Pufu, A. Yarom, *Phys. Rev.* **D78** (2008) 066014. [arXiv:0805.1551].
- [20] V. Balasubramanian, P. Kraus, *Commun. Math. Phys.* **208**, 413-428 (1999). [hep-th/9902121].
- [21] S. de Haro, S. N. Solodukhin, K. Skenderis, *Commun. Math. Phys.* **217**, 595-622 (2001). [hep-th/0002230].
- [22] John P. Boyd, "Chebyshev and Fourier Spectram Methods (2<sup>nd</sup> Edition)," New York: Dover (2001) 688 p.
- [23] M. Luzum, P. Romatschke, *Phys. Rev.* **C78** (2008) 034915. [arXiv:0804.4015].
- [24] M. Luzum, P. Romatschke, *Phys. Rev. Lett.* **103** (2009) 262302. [arXiv:0901.4588].
- [25] H. Song, S. A. Bass, U. Heinz, *Phys. Rev.* **C83** (2011) 054912. [arXiv:1103.2380].
- [26] H. Niemi, G. S. Denicol, P. Huovinen, E. Molnar, D. H. Rischke, *Phys. Rev. Lett.* **106** (2011) 212302. [arXiv:1101.2442].
- [27] M. Strickland, [arXiv:1106.2571].
- [28] A. Rebhan, D. Steineder, [arXiv:1106.3539].
- [29] J. R. Bhatt, H. Mishra, V. Sreekanth, *JHEP* **1011** (2010) 106. [arXiv:1011.1969].
- [30] M. Martinez, M. Strickland, *Phys. Rev.* **C78** (2008) 034917. [arXiv:0805.4552].